Article

Adsorption Kinetics of NO$_2$ Gas on Pt/Cr-TiO$_2$/Pt-Based Sensors

Azhar Ali Haidry [1,2,3,*], Qawareer Fatima [1], Ahmar Mehmood [1], Asim Shahzad [1], Yinwen Ji [1,2] and Bilge Saruhan [4]

[1] College of Materials Science and Technology, Nanjing University of Aeronautics and Astronautics, Nanjing 211100, China; fatimaqawareer@gmail.com (Q.F.); ahmar.mehmood@gmail.com (A.M.); asimshahzad@nuaa.edu.cn (A.S.); yinwen.ji@nuaa.edu.cn (Y.J.)
[2] Key Laboratory of Materials Preparation and Protection for Harsh Environment, Ministry of Industry and Information Technology, Nanjing 211100, China
[3] Department of Physics, University of Okara, 2 KM Multan Road Renala Khurd by-Pass, Okara 56300, Pakistan
[4] German Aerospace Center (DLR), Institute of Materials Research, Linder Hoehe, 51147 Cologne, Germany; bilge.saruhan@dlr.de
[*] Correspondence: aa.haidry@nuaa.edu.cn; Tel.: +86-130-2341-1227

Abstract: Metal oxides are excellent candidates for the detection of various gases; however, the issues such as the limited operating temperature and selectivity are the most important ones requiring the comprehensive understanding of gas adsorption kinetics on the sensing layer surfaces. To this context, the present study focuses mainly on the fabrication of a Pt/Cr-TiO$_2$/Pt type sensor structure that is highly suitable in reducing the operating temperature (from 400 to 200 °C), extending the lower limit NO$_2$ gas concentration (below 10 ppm) with fast response (37 s) and recovery (24 s) times. This illustrates that the sensor performance is not only solely dependent on the nature of sensing material, but also, it is significantly enhanced by using such a new kind of electrode geometry. Moreover, Cr doping into TiO$_2$ culminates in altering the sensor response from n- to p-type and thus contributes to sensor performance enhancement by detecting low NO$_2$ concentrations selectively at reduced operating temperatures. In addition, the NO$_2$ surface adsorption kinetics are studied by fitting the obtained sensor response curves with Elovich, inter-particle diffusion, and pseudo first-order and pseudo second-order adsorption models. It is found that a pseudo first-order reaction model describes the best NO$_2$ adsorption kinetics toward 7–170 ppm NO$_2$ gas at 200 °C. Finally, the sensing mechanism is discussed on the basis of the obtained results.

Keywords: adsorption kinetics; NO$_2$ sensors; titanium dioxide; p-type semiconductors; second order adsorption model

1. Introduction

The detection of oxides of nitrogen (NO and NO$_2$) is highly demanding, as the reducing and oxidizing nature of these gases may yield sensor signals in the opposite directions. In the course of the previous two decades, the outdoor concentration of NO$_2$ gas has been increased particularly due to environmental pollution caused by increased transport and industrial human activities; therefore, its consequences affect human health. Some people with bronchitis/asthma are particularly sensitive to NO$_2$, which causes lung irritations and thus leads to breathing difficulties [1–4]. Furthermore, NO$_2$ is a highly perilous gas for the human and environment as well because of its threshold limit value (TLV), which is about 3 and 5 ppm for 8 h and 15 min (this is estimated for the time-weighted average) [5]. In fact, even the inhalation of low concentrations of NO$_2$ by humans can cause severe damage to the respiratory tract, thus leading to lung cancer. Therefore, the allowed short-time exposure of NO$_2$ gas concentration has been reduced to 1 ppm by the Occupational Safety and Health Administration (US). However, the conventional TLV (as of 2018) is still much lower (≈0.2 ppm). Hence, researchers around the globe are striving to discover new

possible solutions for the detection of NO_2 with high accuracy, sensitivity, and selectivity to avoid any kind of expected danger to humans and the environment [6].

Semiconducting metal oxides (MOx) offer sensing ability in a large variety. However, some may suffer from high cross-sensitivity to many environmental gases [7–10]. In this regard, it is found that TiO_2 is one of the potential candidates for NO_2 sensing and is preferred over other MOx materials due to its low-cost fabrication and chemical stability under harsh and humid environment [11–13]. Yet, the high operating temperature (200–600 °C) of the TiO_2-based sensors has been depreciating their widespread use. The cost and complexity of conventional sensors increase due to the high power consumption, as they require a heater (generally resistive) at the sensing material. Therefore, there is a need for NO_2 gas sensors with improved sensing properties at relatively lower operating temperatures to reduce the power consumption and consequently the cost of sensor device. Recent studies showed that TiO_2 with low-dimensional morphology (for example, nanowires and nanotubes) offer excellent opportunity for reducing the operating temperature [14–17]. However, these nanostructured material-based gas sensors with finer circuitry still have trouble with long-term stability issues. Ultimately, from the commercial point of view, the advanced manufacturing procedures (e.g., use of electron beam lithography and focused ion beam) results in high-cost gas sensor devices.

In general, the response of a gas sensor consists of two functions, receptor and traducer. The receptor (sensing material) enables the identification of gas concentrations by their corresponding interactions. In return, this prompts the relative change in the electrical transport property of the sensing material. Then, the metallic electrodes of the transducer part transfer this change into an electrical output signal. If the transducer function is not properly designed, then the sensor may produce an improper output signal. Importantly, the recent progress in gas sensor is primarily focused on the improvement of receptor function (i.e., the sensing material), while the pre-eminent role of transducer function has been ignored and rarely investigated. Contemporary studies on the effect of transducer function (the role of electrode material, its fabrication methods, its geometry and gap size) have shown that the sensor response can be significantly improved by tuning the transducer properties [18–22]. Recently, our group has proved that a novel sandwiched type configuration ($Pt/TiO_2/Pt$) with top–bottom electrodes can produce fast and highly sensitive response toward NO_2 gas and hence reduce the optimal operating temperature from 400 to 200 °C [23].

The present study reports the implementation of sandwiched-type sensor configuration ($Pt/TiO_2/Pt$) for NO_2-oxidizing gas. The effects of TiO_2 doping with chromium (Cr-TiO_2) are investigated on the basis of crystal structure and layer morphology but also when sandwiched between two Pt electrodes after heat treatment. Ultimately, the NO_2 adsorption mechanism of pristine TiO_2 and Cr-TiO_2 with such configuration is interpreted based on the data obtained.

2. Materials and Methods

The sensors were fabricated in three steps (as shown in Figure 1) via the sputtering deposition technique. Firstly, 300 μm wide and 200 nm thick bottom Pt electrodes (BE) were patterned on alumina substrates via sputter coater (BALTEC, Hallbergmoos, Germany). On the patterned BEs, 2 μm thick TiO_2 or Cr-TiO_2 sensing layers with a columnar structure were deposited by reactive magnetron sputtering from Ti targets (99.95% purity) or Ti and Cr targets (99.99% purity), respectively. The sputtering equipment Z400 (from SVS, Gilching, Germany) allows reactive sputtering from multiple metallic or ceramic sources (targets) under a mixture of 23 sccm (standard cubic centimeter) inert argon (99.999% purity) and 06 sccm reactive oxygen (99.995% purity) flow. Subsequently, as the final step, the top Pt-electrodes (TEs) were deposited as a cross-bar pattern to the bottom Pt electrodes. The width of both the top and bottom electrodes is kept fixed in order to only elucidate the effect of Cr doping on the sensing mechanism.
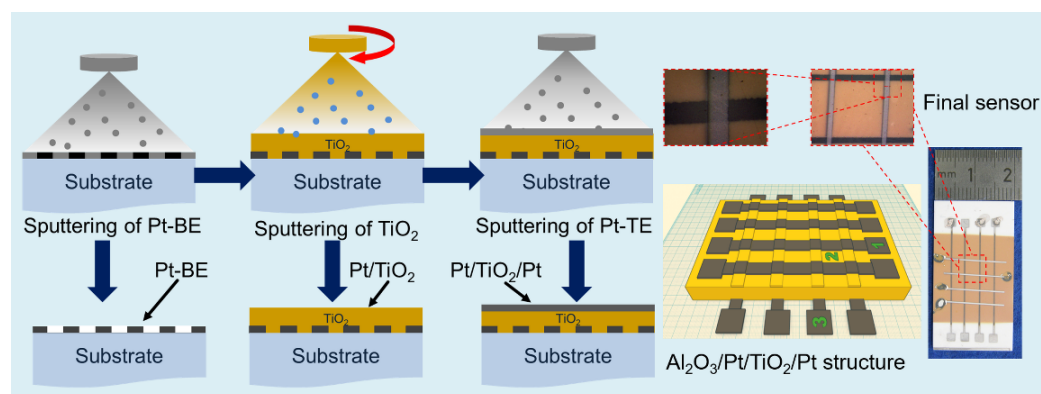
Figure 1. The schematics showing the steps to fabricate Pt/TiO$_2$/Pt-based sensors. The figure also includes the real photograph of one of the real sensors (photos at the right hand-side) fabricated in our lab with the procedure mentioned in the experimental part and optical images of the Pt/TiO$_2$/Pt based cross-bars in the insets.

During the deposition of sensing layers, several other substrates were placed inside the chamber for basic characterization: for instance, sapphire discs of 13 mm diameter (for XRD) and 20 × 20 mm silicon (Si) substrates (for EDX analysis). Thus, the obtained analyses results were free of any interference of Pt from platinum circuitry and Al from Al$_2$O$_3$ substrates. Finally, the sensing structures Pt/TiO$_2$/Pt were post-deposition annealed for 3 h under static air conditions at 800 °C (ramping/heating rate of 6.6 °C per min) in a furnace from HERAEUS Instruments (Hanau, Germany).

The crystal structural analysis was performed in standard Bragg–Brentano geometry by using an X-ray diffractometer XRD-D5000 from SIEMENS AG (Munich, Germany), with a CuKα radiation ($\lambda_{\mathrm{CuK}\alpha}$ = 0.15418 nm) and the graphite curved monochromator. For the quantitative analysis, the measured θ/2θ spectra from the 23° to 87° 2θ range were compared with the standard anatase (PDF 21-1272) and rutile (PDF 21-1276) phases. The morphology of the samples (both surface and cross-sections) was investigated by a field effect scanning electron microscope FE-SEM ULTRA 55 equipped with a built-in energy dispersive spectrometer (EDS) having an X-Ray Fluorescence Analyzer MESA 500 from ZEISS AG (Jena, Germany).

The gas-sensing tests of the Pt/TiO$_2$/Pt-based sensors were performed in a sensor and catalyst characterization unit SESAM (German Aerospace Center, Cologne, Germany), which is fully computer-controlled with custom-made LabVIEW software. The SESAM test unit is comprised of MFC-647b type mass flow controllers (MKS Instruments GmbH, Munich, Germany). The unit has the capability of directing eight various kinds of gases simultaneously via eight-channel flow into the gas mixing chamber made of Quartz-glass recipient, which is permanently placed inside a CARBOLITE tube furnace. The setup enables measuring the high resistance ≈10^{11} Ω of the sensing layer and signal noise is negligible due the usage of a triaxial cable and sensitive resistance measuring source meter Keithley 2635A (Keithley Instruments GmbH, Germering, Germany). The sensors are contacted with thin Pt wires using silver paste solder. During the gas sensing tests, the gas flow rate was kept constant at 400 mL/min, and a constant voltage of 1 V (DC bias) was applied. All instruments included in this unit are controlled with the LabVIEW program.

3. Results and Discussion

3.1. Characterization

In the present case, the coatings were ex situ annealed at 800 °C; contradicting with previous reports [24,25], it can be seen that only anatase phases are present in undoped TiO$_2$ coatings, whereas in Cr-TiO$_2$ coatings, both anatase (PDF 21-1272) and rutile (PDF 21-1276) phases are present in Figure 2, which is in good agreement with [26,27]. From the XRD diffraction patterns, it is notable that the following anatase (101), (004), (200), (101) and

rutile (110), (101), (211) and (220) peaks are present. For anatase phases, the peaks are found at 2θ values of 25.41°, 37.76°, 48.10°, and 53.88°, whereas the peaks corresponding to the rutile phase are observed at 2θ values of 27.44°, 36.06°, and 41.18°. It is very interesting to note that the peak of A (004) is comparatively higher than that of the A (101) phase. For the powder diffraction patterns, the A (101) peak of TiO_2 is higher than the other peaks, which contradicts the above XRD diffractograms, as shown in Figure 2. This scenario happens due to the corundum substrate C [0006], where the crystallites assimilate preferentially following the substrate crystals orientations. From the previous reports, one can anticipate an anatase to rutile transformation for undoped TiO_2 at annealing temperature higher than 800 °C. However, for Cr-TiO_2 coatings, this phase transformation already exists at 800 °C, which is in good agreement with the previous reports [28–30]. A slight shift in the reflections of TiO_2 in the above X-ray diffraction patterns has been observed (Figure 2), which indicates Cr integration into the TiO_2 matrix. Furthermore, no significant changes in the values of lattice parameters are anticipated, which is most probably due to the minor variation in the ionic radii of Cr (0.61 Å) and Ti (0.60 Å). The weight fraction of anatase phase W_A(%) was estimated with the help of Spurr–Mayer's equation for A(101), A(004), and R(110) peaks. The detected weight fraction of anatase is 100 wt % in undoped TiO_2, while for Cr-doped TiO_2, the respective wt % of anatase phase A(101):R(110) and A(004):R(110) W_A(%) is ≈64 wt % and ≈23, respectively (the estimation error with this method is 10%). Thus, one can infer from the quantitative analysis that Cr significantly promotes the phase transformation from anatase to rutile. In addition, metallic Cr and its secondary phases are absent, which affirm that Cr segregates into TiO_2 instead of forming metallic or secondary oxides (e.g., Cr_2O_3).
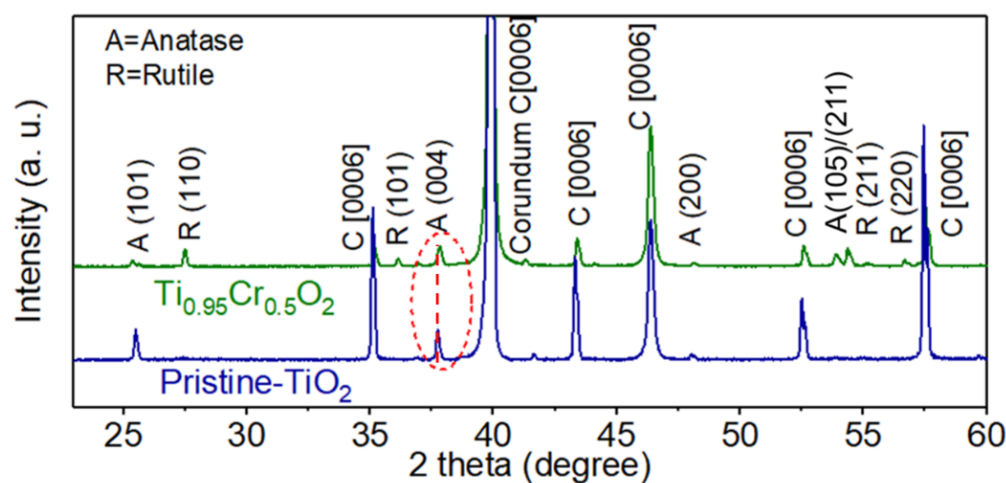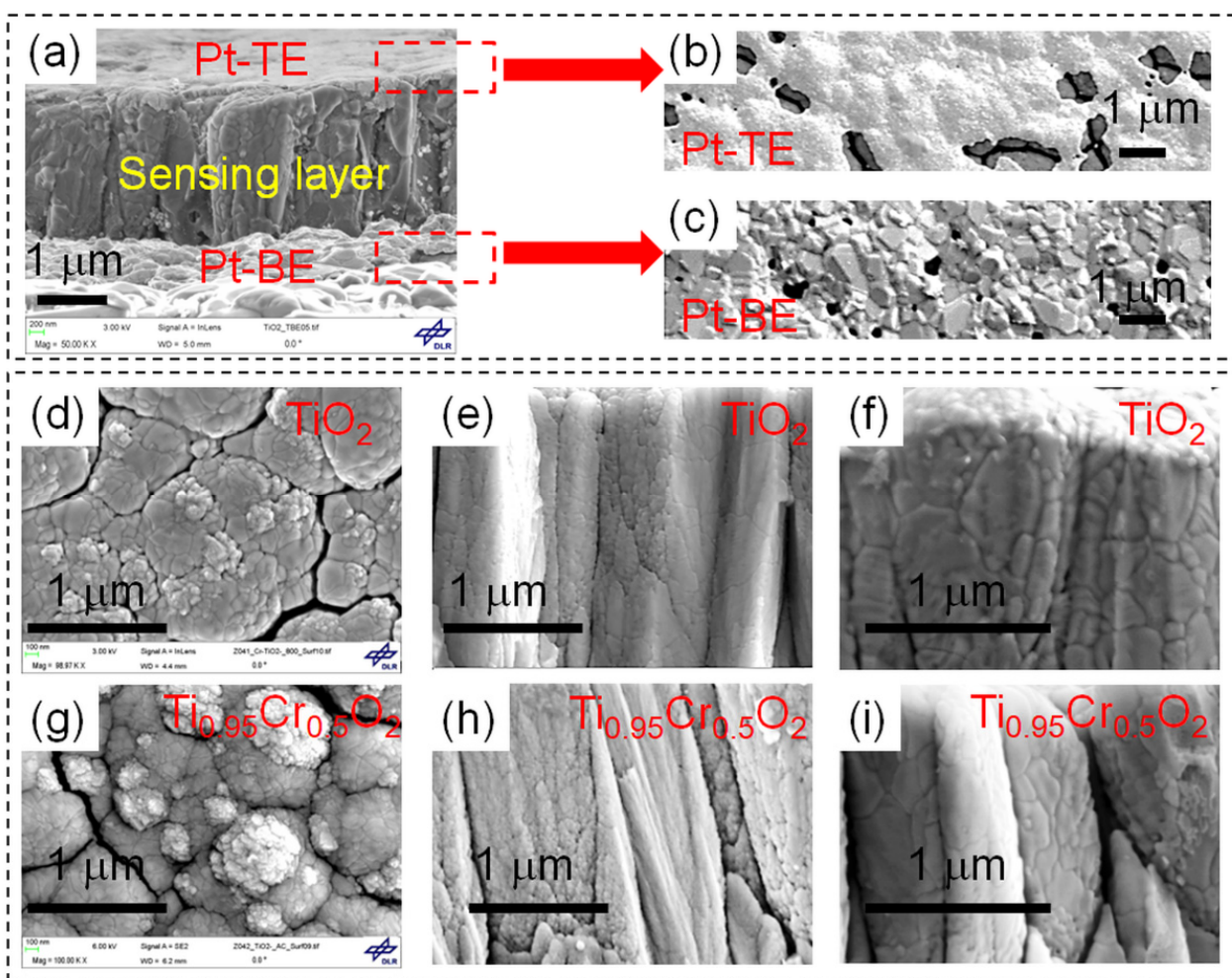

Figure 2. The X-ray diffractograms of the pristine TiO_2-sensing layer and $Ti_{0.95}Cr_{0.5}O_2$-sensing layer deposited on corundum [0006] substrate and annealed at 800 °C.

From the microstructure and compositional analysis of the sensor structure in Figure 3a–c, it is observed that both electrodes show different morphology but are highly stable and do not vanish or crack even after annealing at 800 °C [31]. The Pt layer crystallized with the average faceted grain size of ≈150–200 nm for bottom electrodes and ≈100–150 nm for top electrodes. There are pores (average estimated pore size is ≈350–400 nm) in the top electrodes, which promotes the gas diffusion to the sensing layer surface whereas the pores size in bottom electrode is relatively smaller (≈200–300 nm), and its accumulation is highly in compliance with the substrate even without using the supportive layer for adhesion purpose [32].

A typical micro columnar structure of the sensing layer is observed with excellent adhesion [33,34]. From Figure 3d–i, it can be seen that these vertical columnar structures are around 2 μm in height. After annealing at 800 °C, the grains (amorphous and finely dense in as-deposited form) on the top surface become centered, and these columnar structures

transform to crystalline structures; see Figure 3d,g. There is a formation of occasional nanostructured grains existing as pumps or nodules (average size of ≈70–80 nm) grown on the surface. It can be seen in the SEM images that the average bottom diameters of these columns show an irregular trend. For instance, undoped coatings show an average value of ≈400–520 nm, while for Cr-TiO$_2$ coatings, the estimated average diameter of the columns is smaller (≈300–430 nm). From Figure 3g–i, it is observable that there are a significant number of voids and cracks, which increased in the case of Cr-doped TiO$_2$ films as compared to pristine TiO$_2$ layer Figure 3d–f. The voids size varies from 100 to 300 nm for both coatings. However, the widening of these cracks and voids after annealing at 800 °C is more significant in Cr-TiO$_2$ [35].

Figure 3. The scanning electron microscope (SEM) analysis of both the coatings. The cross-sectional micrograph of the Pt/TiO$_2$/Pt structure (**a**) along with surface topography of Pt-TE (**b**) and Pt-BE (**c**). The surface topographical and cross-sectional micrographs of the pristine TiO$_2$ sensing layer (**d–f**) and Ti$_{0.95}$Cr$_{0.5}$O$_2$ (**g–i**) sensing layer deposited on corundum [0006] substrate and annealed at 800 °C. The color mapping of the various elements (Pt, Ti, O and Cr), showing the Cr incorporation into the TiO$_2$ sensing layer.

From the elemental compositional studies with EDX, it was found that the Cr contents (relative to Ti) in the doped coatings are about 0.5 wt % (Pt/Ti$_{0.95}$Cr$_{0.5}$O$_2$/Pt). The EDX analysis confirms the transformation of non-stoichiometric TiO$_{2-x}$ to near stoichiometric TiO$_2$ after annealing at 800 °C. From Figure 4, it can be seen that there is a diffusion of Pt top and bottom electrodes into the depth of several nanometers into the sensing layer, which is caused by thermally induced Pt atoms into the sensing layer during the annealing

process at 800 °C. Furthermore, it was affirmed by point analysis that the interdiffusion rate is higher at the bottom Pt/TiO_2 interface than at the top interface.
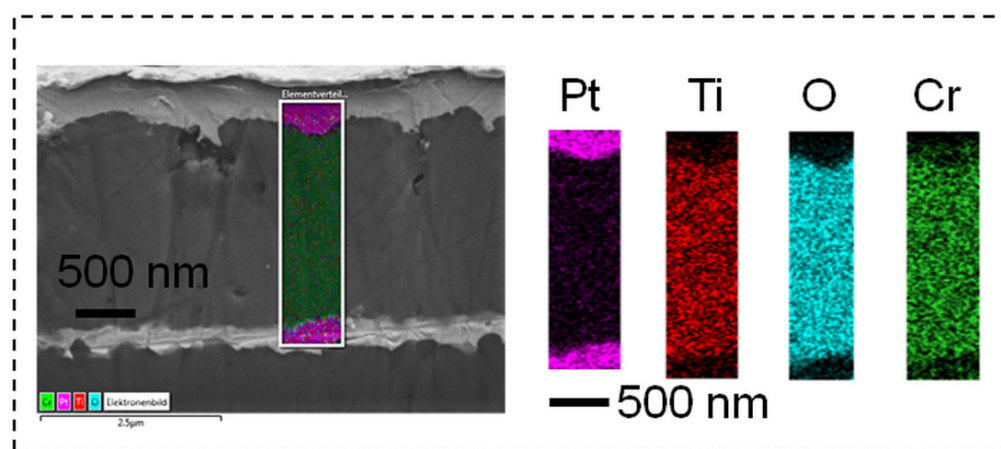

Figure 4. The color mapping of the various elements (Pt, Ti, O, and Cr), showing the Cr incorporation into the TiO_2 sensing layer.

From the GDOES analysis shown in Figure 5, it is noticeable from the variation in quantitative elemental distribution profile that both the as-coated samples consist of a highly non-stoichiometric TiO_{2-x} layer as the O 130 has a decreasing trend, while Ti 399 has an increasing trend; see Figure 5a,b. The figure also shows that the bottom part of the sensing layer is rich in metallic Ti 399. Stoichiometric films are formed after annealing at 800 °C with both concentrations, O 130 and Ti 399, has become constant. It is critical to note that the Ti:O ratio in the region near the bottom Pt/TiO_2 interface is still non-stoichiometric, and it is rich in metallic Ti, which is in good agreement with the EDX analysis. However, this Ti:O ratio is about $\approx 0.80:2.10$; thus, one can conclude that the gradient of O 130 concentration holds even after 800 °C heat treatment (Figure 5c,d). This is also affirmed by the Pt 266 peaks in the annealed samples, which showed extended inclination into TiO_2 from the bottom electrode; such observations were also mentioned in previous reports [36].
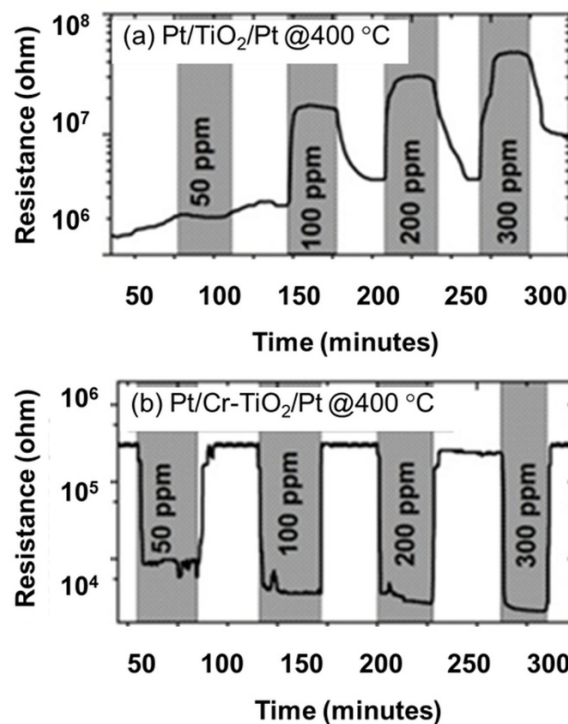
3.2. Sensor Performance

The comparative sensing performance of the pristine TiO_2 sensing layer and $Ti_{0.95}Cr_{0.5}O_2$ (we simply mention it with $Cr-TiO_2$) are shown in Figure 6. It is found that undoped TiO_2 exhibited a typical n-type sensor response ($S_{Rn} = R_{NO2}/R_{air}$), while there was an inverse p-type response ($S_{Rp} = R_{air}/R_{NO2}$) for the Cr-doped TiO_2 based sensor when exposed to a certain concentration of NO_2 gas; here, R_{air} and R_{NO2} indicate saturated resistances in the air and NO_2 gas, respectively. A low baseline resistance in air was observed for the $Pt/Cr-TiO_2/Pt$ sensor ($\approx 3.5 \times 10^5$ ohm) compared to that of the undoped TiO_2 sensor ($\approx 2.6 \times 10^6$ ohm) at 400 °C shown in Figure 6. The inimitable sensing responses of both prepared sensors toward 50–300 ppm of NO_2 at 400 °C is illustrated in Figure 7a. Furthermore, it is evident from Figure 7a that the Cr-doped TiO_2 sensor showed a superior response toward NO_2. For example, the $Pt/TiO_2/Pt$-based sensor showed about $S_{Rn} \approx 1.58$, while the $Pt/Cr-TiO_2/Pt$ based sensor showed about $S_{Rp} \approx 33.24$ toward 50 ppm NO_2 at 400 °C. In both cases, the sensor response increased with the NO_2 gas concentration. However, a significant drift in the baseline resistance is found for $Pt/TiO_2/Pt$-based sensor due to incomplete recovery, but then, $Pt/Cr-TiO_2/Pt$-based sensors showed excellent response with full recovery after the NO_2 gas is off. In addition, for the sensors based on the $Pt/Cr-TiO_2/Pt$ structure, the sensor response values increased as the operating temperature decreased from 400 to 200 °C, compared with $Pt/TiO_2/Pt$-based sensors that showed the best response at 400 °C while observing the decreasing trend with an operating temperature decrease in the same range. One can infer that Cr incorporation in the Ti-O

matrix can significantly decrease the operating temperature of the sensor and thus require less power consumption when designing a gas sensor for real-life applications.
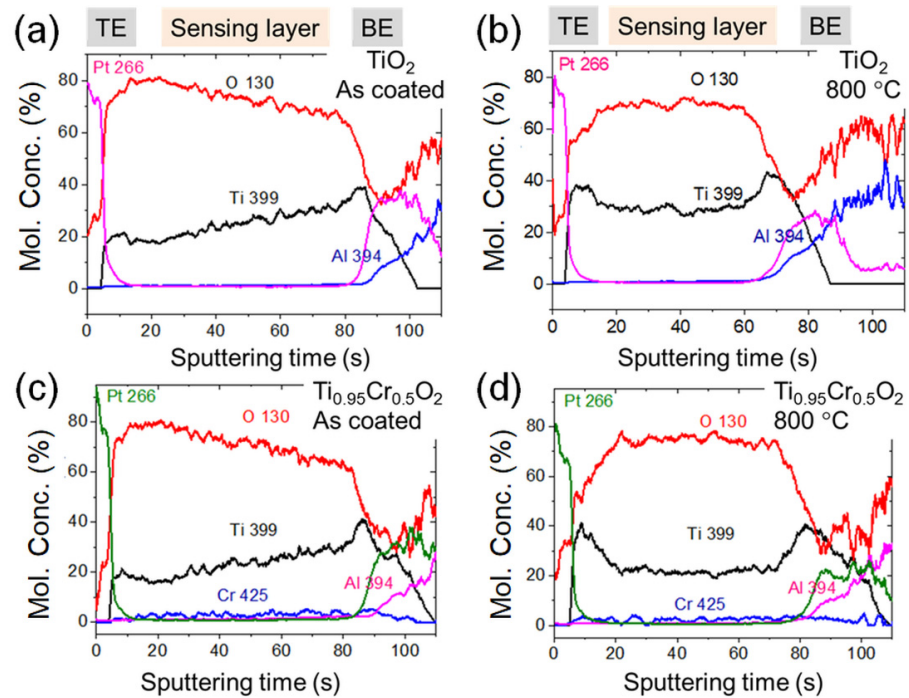
Figure 5. The glow discharge optical emission spectroscopic plots showing the quantitative analysis of evolution of composition of the various elements (Pt, Ti, O, and Cr) in the pristine TiO_2 sensing layer (**a**,**b**) and $Ti_{0.95}Cr_{0.5}O_2$ (**c**,**d**) both as-deposited and annealed at 800 °C. The color elemental composition shows the defected sensing layer in the as-deposited state and stoichiometric state at 800 °C annealing with evidence of Cr incorporation into the TiO_2 sensing layer.

Figure 6. The dynamic responses of $Pt/TiO_2/Pt$ and $Pt/Cr-TiO_2/Pt$ sensors measured at 400 °C toward different concentrations (50, 100, 200, 300 ppm) of NO_2 gas.
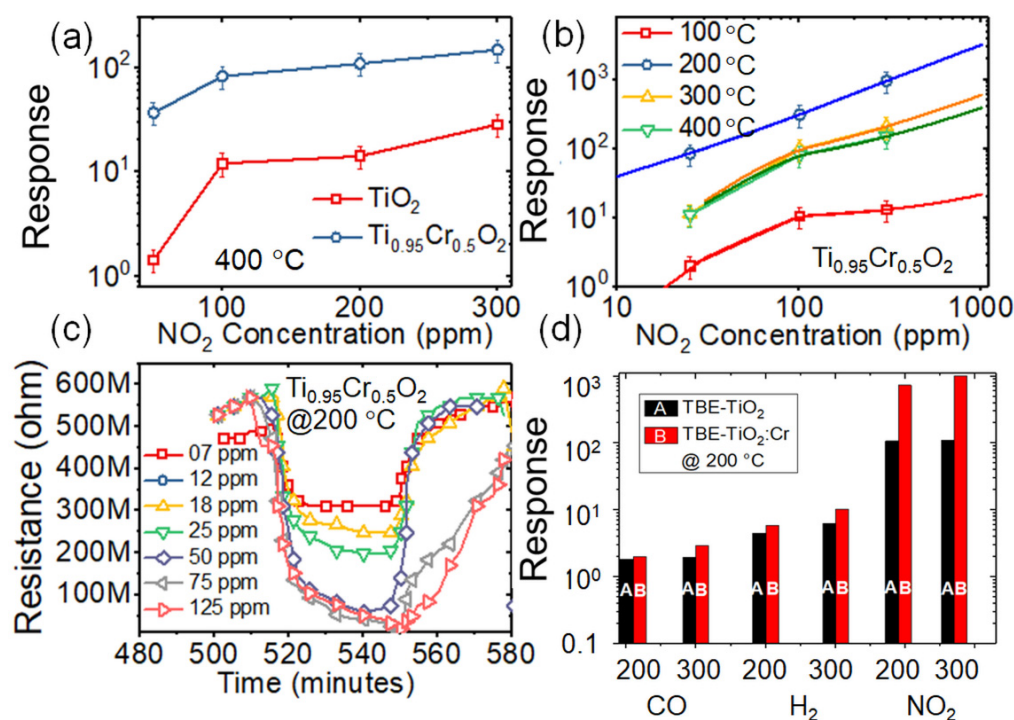
Figure 7. The comparative sensing performance of the $Pt/TiO_2/Pt$ and $Pt/Cr-TiO_2/Pt$ (**a**) sensors measured at 400 °C and annealed at 800 °C. Further sensing analysis of $Pt/Cr-TiO_2/Pt$ sensors at various temperatures 100 °C, 200 °C, 300 °C, and 400 °C (**b**), the dynamic responses of the $Pt/Cr-TiO_2/Pt$ sensor measured at 200 °C toward low concentrations (7, 12, 18, 25, 50, 75, and 125 ppm) of NO_2 gas (**c**), the selectivity of the $Pt/Cr-TiO_2/Pt$ sensor toward NO_2 again H_2, and CO reducing exhaust gases (**d**).

Based on the aforementioned superior performance, the further analysis was done on $Pt/Cr-TiO_2/Pt$-based sensors. It is well-known that the response of the gas sensor is strongly dependent on the gas concentration and operating temperature due to the adsorption/desorption processes of various gases on the surface of the sensing layer. Figure 5b depicts the sensing analysis of $Pt/Cr-TiO_2/Pt$ sensors at various temperatures (100 °C, 200 °C, 300 °C, and 400 °C) toward increasing NO_2 concentration. For the reader's clarity, it is to be noted that in the current study, the actual gas concentration used is 25–400 ppm NO_2, while the curves in the Figure 7b are extrapolated to show the trend of sensor response with gas concentration. The gas-sensing measurements of the $Pt/Cr-TiO_2/Pt$ sensor in Figure 7b show that the maximum response was obtained at 200 °C. Thus, the dynamic sensing responses of the $Pt/Cr-TiO_2/Pt$ sensor toward low concentrations of NO_2 gas were measured at 200 °C. Figure 7c depicts the real-time variation in baseline resistance before and after exposure to 7, 12, 18, 25, 50, 75, and 125 ppm NO_2. The gas sensing measurements showed that the sensor could detect NO_2 gas at a concentration as low as 7 ppm with reproducible signals at 200 °C. The $Ti_{0.95}Cr_{0.5}O_2$ sensor shows the recoverable and reproducible response at 7 ppm NO_2 gas, which indicates that the sensor could detect a low concentration of the NO_2 gas, thus leading to the detection of a broad range of NO_2 concentration (7–400 ppm). To further elaborate, at 200 °C, the response of $Pt/Cr-TiO_2/Pt$ based sensors is about $\approx$212 and 545 toward 50 and 100 ppm, which is higher than the response mentioned in the reports on the TiO_2-based sensors [37–40]. Furthermore, the $Pt/Cr-TiO_2/Pt$ sensors showed remarkable sensing characteristics such as response and recovery times (estimated for 90% resistance change). For instance, at 200 °C, the response and recovery times toward 100 ppm are 37 s and 24 s respectively, which indicates the fast response and recovery of the sensors.

3.3. Adsorption Kinetics

It is well-established that TiO$_2$ offers multifunctional properties [41], and while designing a gas sensor, it is of utmost importance to get scientific insights about the gas adsorption kinetics onto the surface of the sensing layer. In our previous report, we have shown that room temperature hydrogen adsorption onto an ordered mesoporous TiO$_2$ surface is mainly governed by the pseudo second-order rate equations. However, in the present case, we chose the NO$_2$ adsorption fitting at 200 °C, which is the optimum temperature to obtain the highest response, and found that the pseudo first-order model fits well with the obtained dynamic responses. In fact, the obtained adsorption regressions were fitted with the Elovich model (EM), inter-particle diffusion model (IPD), Lagergren's pseudo first order (or simply pseudo first order—PFO), and Ho's pseudo second-order (or simply pseudo second-order—PSO) models.

For the Elovich model, in the adsorption regression expression (Equation (1)), we consider that the surface coverage of NO$_2$ onto the sensor layer is θ_t (at time t), the adsorption and desorption are represented by a and b respectively.

$$\frac{d\theta_t}{dt} = a\, e^{-b\theta_t} \tag{1}$$

Under the condition that $\theta_t = 0$ at $t = 0$, the integration of the Equation (1) results in Equation (2).

$$\theta_t = \frac{1}{b}\ln(t + t_0) + \frac{1}{b}\ln(t_0) \tag{2}$$

If the condition $t \gg t_0$ is valid, then one may write:

$$\theta_t = \frac{1}{b}\ln(ab) + \frac{1}{b}\ln(t). \tag{3}$$

After fitting the obtained data with the Elovich model, we found an irregular trend in the R^2 values for each fitting curve. The R^2 values range from 0.33 to 0.66, which means that the adsorption does not follow Equation (3) of the Elovich model; the fitting of these curves can be seen in Figure 8a.

$$\theta_t = k_{id}t^{0.5} + C_i \tag{4}$$

As demonstrated in Figure 8b, next, the response data were fitted with the inter-particle diffusion (IPD) model, which is generally governed with molecular or ionic transport at the grain boundaries of the polycrystalline sensing layer, and its fitting is done by using Equation (4). Here, θ_t is the surface coverage of NO$_2$ gas adsorbed on the sensing layer, C_i is the inter-particle boundary width and directly linked with the thickness of the sensing layer, and k_{id} is the inter-particle diffusion constant. Since our sensing layers are polycrystalline in nature but not purely a porous layer, thus, the IPD fitting values of R^2 (0.49–0.88) are also not in accordance with the linearity of the model fitting; see Figure 8b.

$$\frac{d\theta_t}{dt} \cong k_2 \left(\theta_e - \theta_t\right)^n \tag{5}$$

The above equation (Equation (5)) represents the pseudo nth order rate regression. For $n = 1$ and $n = 2$, we can fit the pseudo first-order Figure 8c and pseudo second-order Figure 8d adsorption kinetics. In Equation (5), k_2 is the first-order reaction rate constant, θ_t is the surface coverage at equilibrium, and θ_e is the surface coverage at equilibrium, respectively. The integration of Equation (5) yields the following relationship:

$$\ln(\theta_e - \theta_t) = \ln(\theta_e) - k_2 t. \tag{6}$$

In addition, for PSO, the above equation (Equation (5)) can be solved as:

$$\frac{t}{\theta_t} = \frac{1}{k_3\theta_e^2} + \frac{1}{\theta_e}t. \tag{7}$$
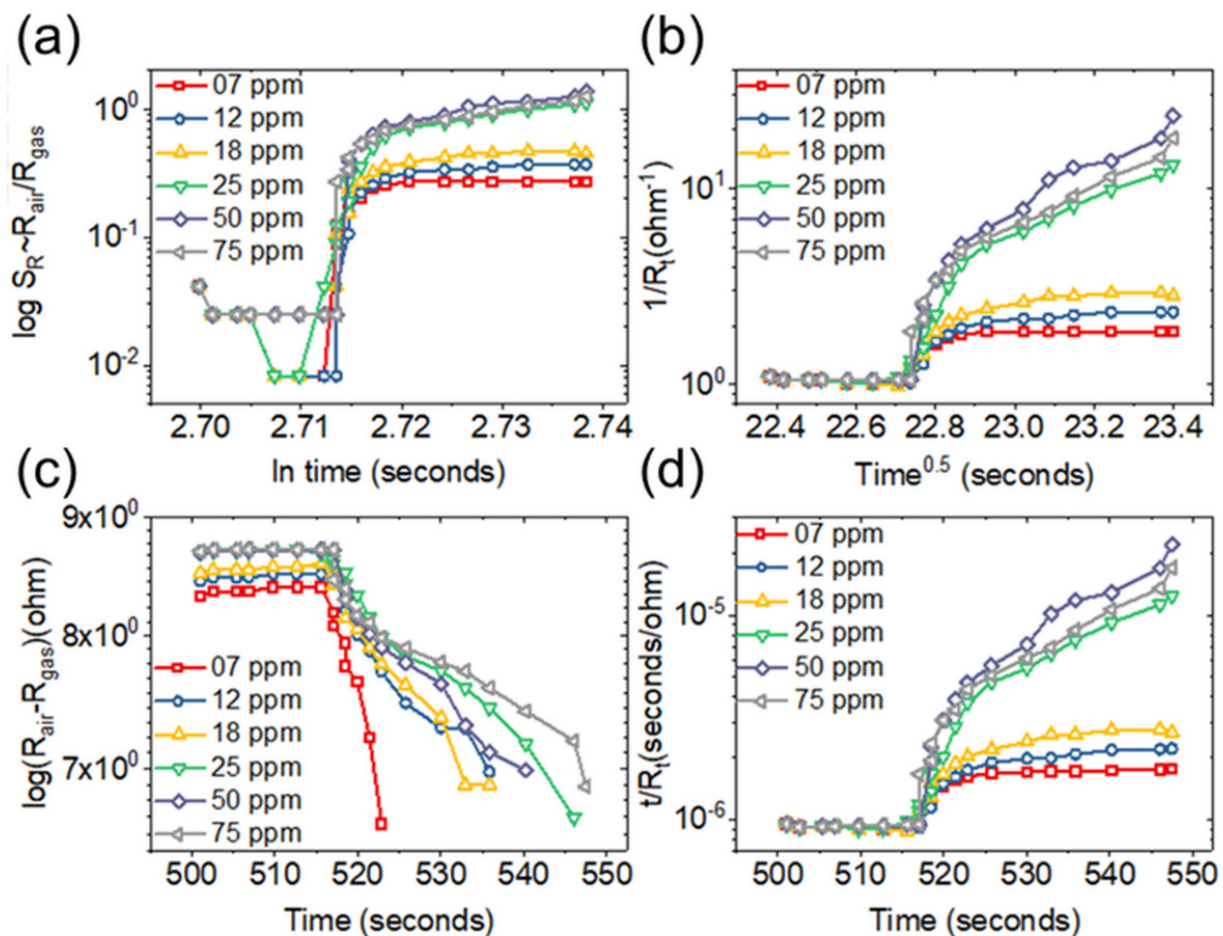
Figure 8. The response and regression analysis of NO$_2$ adsorption (7, 12, 18, 25, 50, and 75 ppm) on the Pt/Cr-TiO$_2$/Pt surface. The original data are shown as color symbols, and their fitting is shown with various color dashed lines. The data were fitted by using the Elovich model (**a**), inter-particle diffusion model (**b**), pseudo first-order model also known as Lagergren's first-order model (**c**) and pseudo second-order model also known as Ho's second-order model (**d**).

Then, the obtained sensor dynamic responses are further fitted with PFO and PSO, as shown in Figure 8c,d. The fitting with PFO is more accurate than PSO as the R^2 values of PFO fall in the range of 0.93–0.97, while for PSO, the R^2 values fall in the range of 0.58–0.89. The R^2 values obtained after the fitting of the data with various models are shown in Table 1 and plotted in Figure 9a. Thus, as given in Figure 9b, we further proceed with the fitting of obtained data with the PFO model, and the estimated reaction parameters are shown in Table 1. Here, the surface coverage at equilibrium θ_e corresponds to the sensor response S$_R$ and reaction constant corresponds to the resistance of the sensor; see Figure 9c. Thus, we can conclude that the PFO model has the highest appositeness to describe the NO$_2$ adsorption on the surface of the Pt/Cr-TiO$_2$/Pt sensor at 200 °C. The values of rate constants k are seven orders of magnitude lower than the saturated sensor resistance in various gas concentrations; however, the surface coverage values (9.03–3866.09) are well pertinent with the experimentally obtained sensor response shown in Figure 9c. Furthermore, the data presented for PFO in Table 1 illustrate that the surface coverage is linearly proportional to the amount of gas adsorption (sensor response) that is also depicted from Figure 8, where its linear fitting is observed with increasing NO$_2$ gas concentrations. Here, the reaction rate is also dependent on the number of adsorption sites and the rate constant k. The reaction constant k is determined, which decreases linearly with gas concentration. This corresponds to the decrease in the sensor's resistance, indicating that the adsorption

reaction in Cr-TiO$_2$ is a pseudo first-order reaction, which is more favorable as compared to the pseudo second-order adsorption reaction, as shown in Figure 8a.

Table 1. The R^2 values obtained with the help of the Elovich model, IPD, PFO, and PSO model. The table also includes the adsorption constants (reaction rate constant and surface coverage) obtained via the PFO model.

| NO$_2$ Concentration (ppm)	R^2 Value				PFO	
	Elovich Model	IPD Model	PFO Model	PSO Model	Reaction Constant	Surface Coverage
7	0.41688	0.49611	0.93143	0.58517	3.26×10^8	9.03404
12	0.33381	0.64163	0.9351	0.67651	1.41×10^8	48.91089
18	0.43138	0.66521	0.96841	0.69388	1.05×10^8	93.6908
25	0.66231	0.88895	0.97402	0.8918	4.93×10^7	678.57839
50	0.41089	0.85677	0.9472	0.85997	2.6×10^7	1450.98803
70	0.39329	0.87706	0.94101	0.88094	1.09×10^7	3866.0941
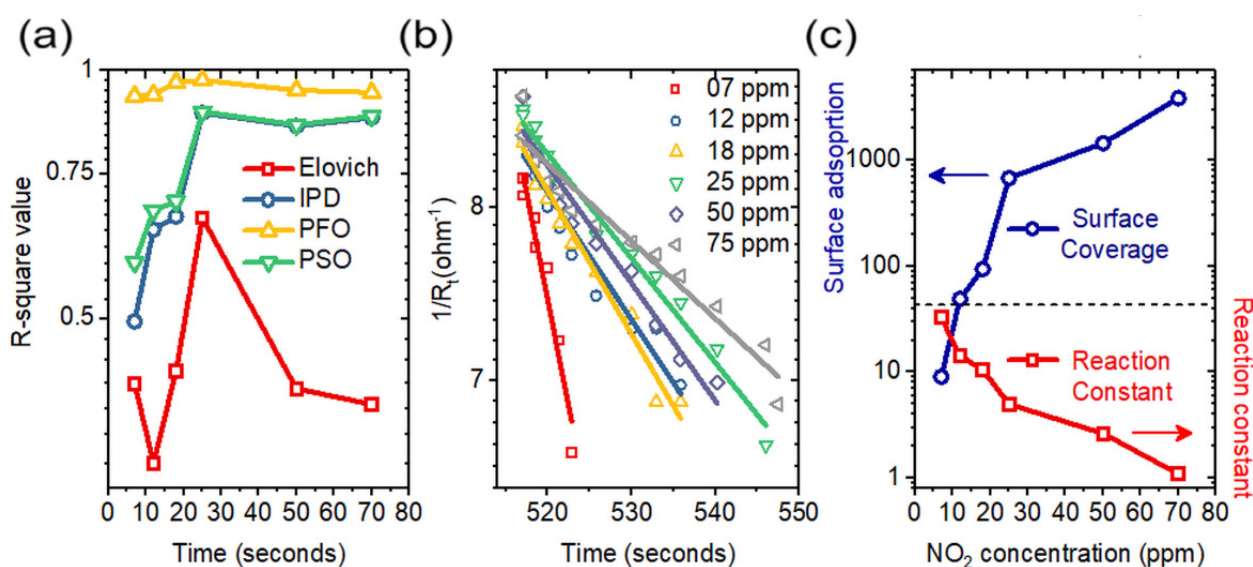
Figure 9. The comparative plot showing the R^2 values for the Elovich, IPD, PFO, and PSO models (**a**), the plot showing the linear fitting of the data by using a pseudo first-order model also known as Lagergren's first-order model (**b**), and the estimated values of its reaction rate constant k (the squared symbols in red color), the values are normalized to 10^7 to make the plot clear to the reader, and the adsorption capacity θ_e (circled symbol in blue color) values are shown in (**c**).

3.4. Sensing Mechanism

The sensing mechanism for NO$_2$ gas onto the TiO$_2$ sensing layer is based on three stages: firstly, the adsorption of gas, secondly, the transfer of charge due to the adsorbed gas, and lastly, desorption of the gas. The surface of the metal oxide (adsorbate) has a natural ability to collect and gather species based on chemicals (adsorbent). As the adsorbate is accessible for air, the oxygen percentage in its molecule (lower than 150 °C) or available ionic phase (higher than 150 °C) can be easily adsorbed, giving a depletion layer by the captured electrons. As shown in Figure 10, the sensing mechanism for NO$_2$ depends on occurrence of the reactions between adsorbate and NO$_2$ gas; this yields an increase or decrease in the resistance value of the sensing layer due to the charge transfer function, as shown by the following Equation (8).

$$\text{NO}_2 \text{ (gas)} + \text{e}^- \rightarrow \text{NO}_2^- \text{ (ads)} \tag{8}$$
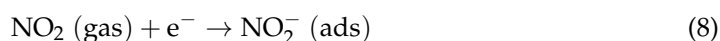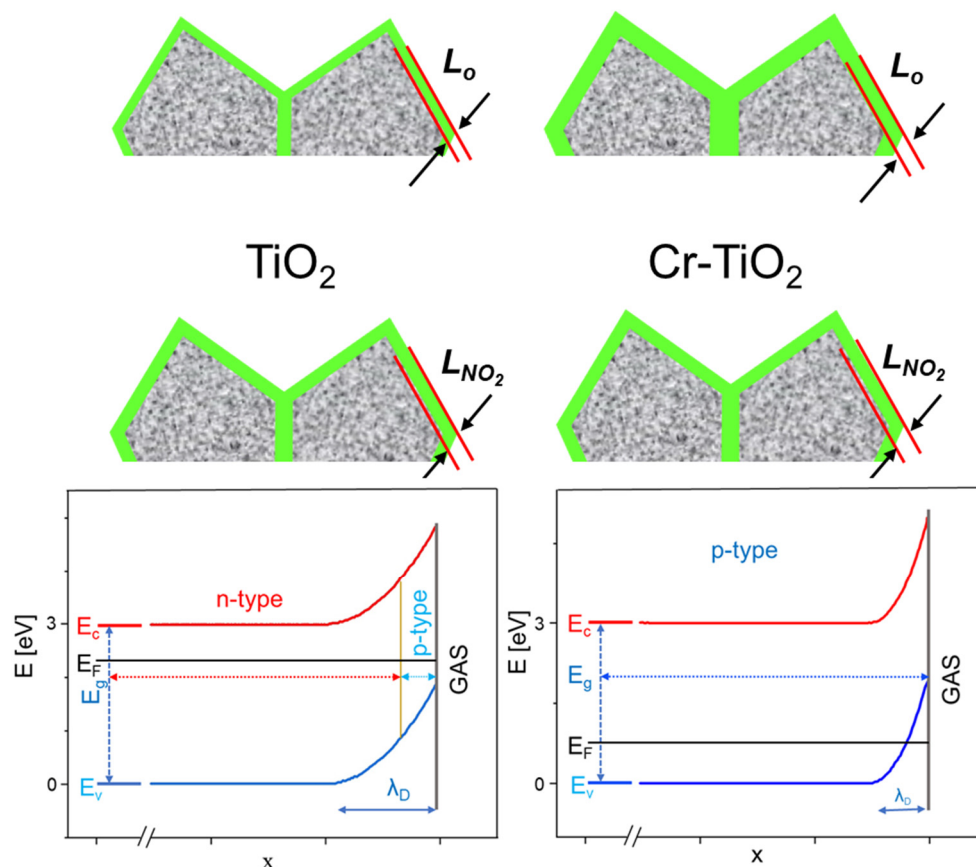
Figure 10. The sensing mechanism of NO_2 adsorption onto pristine (n-type) and Cr-doped TiO_2 (p-type) sensing layers.

If the adsorbate is n-type, the increase in resistance is caused by the NO_2 surface reaction, this is firstly led by the oxygen vacancies V_O that are doubly ionized, and secondly, the encounter between O^-/O^{2-} and NO_2 gas adsorption, as the adsorption of NO_2 is more robust, it dominates the O^-/O^{2-} adsorption. On the other side, the decrease in resistance in the p-type adsorbate is accomplished by an inversion layer which is created by trivalent acceptor-type impurity (e.g., Cr^{3+}). As the chromium Cr^{3+} is doped with the titanium dioxide, it changes the electronic structure of TiO_2 by developing an acceptor level just below the conduction band shown in Figure 10, thus causing the Fermi level to lower down. This variation from n-type to p-type conductivity happens after a certain concentration of Cr^{3+} doping, as in this scenario, the defects found in the acceptor have outnumbered the donor defects, as shown in the Equation (9) below.

$$Cr_2O_3 + \frac{1}{2}O^2 \rightarrow 2Cr'_{Ti} + 2h^{\bullet} + 4O_o^x \qquad (9)$$
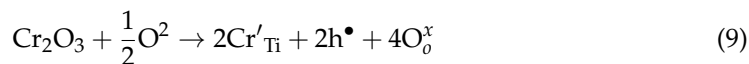
According to the literature, this p-type conductivity is attained by at least 5 at % dopant concentration of Cr in TiO_2 nanopowders. In our case, 2 at % of Cr dopant has already yielded in p-type sensor behavior; also, there are no chromium oxides peaks detected in the XRD patterns. According to XRD analysis, $64 \pm 10\%$ of the anatase phases is found in the undoped TiO_2 that has a marginally higher optical bandgap of 3.2 eV than that of the rutile phase after Cr doping, giving the value of 3 eV in Cr-TiO_2 films. The better sensitivity of NO_2 in Cr-TiO_2 cannot be linked with only this point. This bandgap difference of 0.2 eV can alter the height of the activation energy barrier initiated between the grains (eV_S). In our case, the bandgap values for undoped TiO_2 (0.36 eV) and Cr-TiO_2 (0.35) are not much varied.

4. Conclusions

In this work, we demonstrate a highly sensitive $Pt/Cr-TiO_2/Pt$ sensor design suitable for NO_2 detection with the reduced operating temperatures (200 °C) and lower limit of the NO_2 gas concentrations (7 ppm). The XRD, SEM, EDX, and GDOES analyses confirmed that the dominant anatase A (004) crystal structure was preferentially oriented following the crystal orientation of the substrate, which was a morphology of columnar structured TiO_2 matrix with a column diameter of $\approx$400–520 nm for undoped TiO_2 and a smaller column diameter $\approx$ 300–430 nm for $Cr-TiO_2$ coatings, and the interdiffusion of Pt/TiO_2 specifically more at the bottom interface. The sensor response at 200 °C is relatively high $\approx 1.08 \times 10^3$ toward 300 ppm NO_2 with a response (recovery) time of $\approx$37 s ($\approx$24 s). The adsorption kinetics fitting showed that pseudo first-order reaction regressions are linearly fitted (R^2 value above 0.97) with the obtained sensor responses. The obtained reaction rate (32.60–1.09) and surface coverage (9.03–3866.09) showed comparative trends observed for the sensor resistance and sensor response; however, the rate constant value is 10^7 orders lower than that of the sensor resistance. The sensing mechanism is explained on the basis of surface adsorption kinetics and reduced grain size due to Cr segregation into the Ti-O matrix.

Author Contributions: Conceptualization, methodology and resources, data curation, formal analysis, investigation and writing—original draft, A.A.H.; Formal analysis and writing—original draft, Q.F.; Investigation and writing—review and editing, A.M.; Investigation and writing—review and editing, A.S.; Formal analysis and validation, Y.J.; Writing—review and editing, Project administration and supervision, B.S.; All authors equally contributed to this work. All authors have read and agreed to the published version of the manuscript.

Institutional Review Board Statement: The study was conducted according to the guidelines of the Declaration of German Aerospace Center (DLR), German Academic Exchange Services (DAAD) and Nanjing University of Aeronautics and Astronautics (NUAA). The study was funded and approved by the DLR-DAAD fellowship grants and National Natural Science Foundation of China.

Informed Consent Statement: Not applicable as this study does not include any human and/or animal participants under observation.

Data Availability Statement: The data presented in this study are available on request from the corresponding author. The data are not publicly available due to DLR/DAAD/NUAA confidentiality and privacy.

Conflicts of Interest: The authors declare no competing financial interest.

References

1. Myasoedova, T.N.; Plugotarenko, N.K.; Moiseeva, T.A. Copper-Containing Films Obtained by the Simple Citrate Sol–Gel Route for NO_2 Detection: Adsorption and Kinetic Study. *Chemosensors* **2020**, *8*, 79. [CrossRef]
2. Ueda, T.; Boehme, I.; Hyodo, T.; Shimizu, Y.; Weimar, U.; Barsan, N. Enhanced NO_2-Sensing Properties of Au-Loaded Porous In_2O_3 Gas Sensors at Low Operating Temperatures. *Chemosensors* **2020**, *8*, 72. [CrossRef]
3. Levy, J.I. Impact of residential nitrogen dioxide exposure on personal exposure: An international study. *J. Air Waste Manag. Assoc.* **1998**, *48*, 553–560. [CrossRef]
4. Tomeček, D.; Piliai, L.; Hruška, M.; Fitl, P.; Gadenne, V.; Vorokhta, M.; Matolínová, I.; Vrňata, M. Study of Photoregeneration of Zinc Phthalocyanine Chemiresistor after Exposure to Nitrogen Dioxide. *Chemosensors* **2021**, *9*, 237. [CrossRef]
5. Hjiri, M. Highly sensitive NO_2 gas sensor based on hematite nanoparticles synthesized by sol–gel technique. *J. Mater. Sci. Mater. Electron.* **2020**, *31*, 5025–5031. [CrossRef]
6. Kaur, N.; Zappa, D.; Comini, E. Shelf Life Study of NiO Nanowire Sensors for NO_2 Detection. *Electron. Mater. Lett.* **2019**, *15*, 743–749. [CrossRef]
7. Teoh, L.G.; Hung, I.M.; Shieh, J.; Lai, W.H.; Hon, M.H. High sensitivity semiconductor NO_2 gas sensor based on mesoporous WO_3 thin film. *Electrochem. Solid State Lett.* **2003**, *6*, G108. [CrossRef]

8.   Barsan, N.; Koziej, D.; Weimar, U.; Chemical, A.B. Metal oxide-based gas sensor research: How to? *Sens. Actuators B Chem.* **2007**, *121*, 18–35. [CrossRef]

9.   Sholehah, A.; Faroz, D.F.; Huda, N.; Utari, L.; Septiani, N.L.W.; Yuliarto, B. Synthesis of ZnO flakes on flexible substrate and its application on ethylene sensing at room temperature. *Chemosensors* **2020**, *8*, 2. [CrossRef]

10.   Galstyan, V.; Comini, E.; Ponzoni, A.; Sberveglieri, V.; Sberveglieri, G. ZnO quasi-1D nanostructures: Synthesis, modeling, and properties for applications in conductometric chemical sensors. *Chemosensors* **2016**, *4*, 6. [CrossRef]

11.   Saruhan, B.; Yüce, A.; Gönüllü, Y.; Kelm, K. Effect of Al doping on NO_2 gas sensing of TiO_2 at elevated temperatures. *Sens. Actuators B Chem.* **2013**, *187*, 586–597. [CrossRef]

12.   Haidry, A.A.; Durina, P.; Tomasek, M.; Gregus, J.; Schlosser, P.; Mikula, M.; Truhly, M.; Roch, T.; Plecenik, T.; Pidik, A. Effect of post-deposition annealing treatment on the structural, optical and gas sensing properties of TiO_2 thin films. *Key Eng. Mater.* **2012**, *510–511*, 467–474. [CrossRef]

13.   Gönüllü, Y.; Haidry, A.A.; Saruhan, B. Nanotubular Cr-doped TiO_2 for use as high-temperature NO_2 gas sensor. *Sens. Actuators B Chem.* **2015**, *217*, 78–87. [CrossRef]

14.   Zhang, D.; Fan, Y.; Li, G.; Du, W.; Li, R.; Liu, Y.; Cheng, Z.; Xu, J. Biomimetic synthesis of zeolitic imidazolate frameworks and their application in high performance acetone gas sensors. *Sens. Actuators B Chem.* **2020**, *302*, 127187. [CrossRef]

15.   Yang, X.; Hao, X.; Liu, T.; Liu, F.; Wang, B.; Ma, C.; Liang, X.; Yang, C.; Zhu, H.; Zheng, J.; et al. CeO_2-based mixed potential type acetone sensor using $La_{1-x}Sr_xCoO_3$ sensing electrode. *Sens. Actuators B Chem.* **2018**, *269*, 118–126. [CrossRef]

16.   Abdelghani, R.; Hassan, H.S.; Morsi, I.; Kashyout, A. Nano-architecture of highly sensitive SnO_2–based gas sensors for acetone and ammonia using molecular imprinting technique. *Sens. Actuators B Chem.* **2019**, *297*, 126668. [CrossRef]

17.   Amiri, V.; Roshan, H.; Mirzaei, A.; Neri, G.; Ayesh, A.I. Nanostructured metal oxide-based acetone gas sensors: A review. *Sensors* **2020**, *20*, 3096. [CrossRef] [PubMed]

18.   Shaalan, N.; Yamazaki, T.; Kikuta, T. Effect of micro-electrode geometry on NO_2 gas-sensing characteristics of one-dimensional tin dioxide nanostructure microsensors. *Sens. Actuators B Chem.* **2011**, *156*, 784–790. [CrossRef]

19.   Tamaki, J.; Miyaji, A.; Makinodan, J.; Ogura, S.; Konishi, S. Effect of micro-gap electrode on detection of dilute NO_2 using WO_3 thin film microsensors. *Sens. Actuators B Chem.* **2005**, *108*, 202–206. [CrossRef]

20.   Li, Z.; Yao, Z.; Haidry, A.A.; Plecenik, T.; Grancic, B.; Roch, T.; Gregor, M.; Plecenik, A. The effect of Nb doping on hydrogen gas sensing properties of capacitor-like Pt/Nb-TiO_2/Pt hydrogen gas sensors. *J. Alloys Compd.* **2019**, *806*, 1052–1059. [CrossRef]

21.   Capone, S.; Siciliano, P.; Quaranta, F.; Rella, R.; Epifani, M.; Vasanelli, L. Moisture influence and geometry effect of Au and Pt electrodes on CO sensing response of SnO_2 microsensors based on sol–gel thin film. *Sens. Actuators B Chem.* **2001**, *77*, 503–511. [CrossRef]

22.   Haidry, A.A.; Xie, L.; Wang, Z.; Zavabeti, A.; Li, Z.; Plecenik, T.; Gregor, M.; Roch, T.; Plecenik, A. Remarkable improvement in hydrogen sensing characteristics with Pt/TiO_2 interface control. *ACS Sens.* **2019**, *4*, 2997–3006. [CrossRef] [PubMed]

23.   Haidry, A.A.; Cetin, C.; Kelm, K.; Saruhan, B. Sensing mechanism of low temperature NO_2 sensing with top–bottom electrode (TBE) geometry. *Sens. Actuators B Chem.* **2016**, *236*, 874–884. [CrossRef]

24.   Bakri, A.; Sahdan, M.Z.; Adriyanto, F.; Raship, N.; Said, N.; Abdullah, S.; Rahim, M. Effect of annealing temperature of titanium dioxide thin films on structural and electrical properties. *AIP Conf. Proc.* **2017**, *1788*, 030030. [CrossRef]

25.   Zhang, Q.; Li, C. High Temperature Stable Anatase Phase Titanium Dioxide Films Synthesized by Mist Chemical Vapor Deposition. *Nanomaterials* **2020**, *10*, 911. [CrossRef]

26.   Sertel, B.C.; Efkere, H.I.; Ozcelik, S. Gas Sensing Properties of Cr Doped TiO_2 Films Against Propane. *IEEE Sens.* **2020**, *20*, 13436–13443. [CrossRef]

27.   Su, T.-Y.; Chen, Y.-Z.; Wang, Y.-C.; Tang, S.-Y.; Shih, Y.-C.; Cheng, F.; Wang, Z.M.; Lin, H.-N.; Chueh, Y.-L. Highly sensitive, selective and stable NO_2 gas sensors with a ppb-level detection limit on 2D-platinum diselenide films. *J. Mater. Chem. C* **2020**, *8*, 4851–4858. [CrossRef]

28.   Lee, S.P. Electrodes for semiconductor gas sensors. *Sensors* **2017**, *17*, 683. [CrossRef]

29.   Li, Z.; Xing, L.; Zhang, Z. Photocatalytic Properties of Columnar Nanostructured Films Fabricated by Sputtering Ti and Subsequent Annealing. *Adv. Mater. Sci. Eng.* **2012**, *2012*, 413638. [CrossRef]

30.   Spurr, R.A.; Myers, H. Quantitative analysis of anatase-rutile mixtures with an X-ray diffractometer. *Anal. Chem.* **1957**, *29*, 760–762. [CrossRef]

31.   Lyson-Sypien, B.; Czapla, A.; Lubecka, M.; Gwizdz, P.; Schneider, K.; Zakrzewska, K.; Michalow, K.; Graule, T.; Reszka, A.; Rekas, M.; et al. Nanopowders of chromium doped TiO_2 for gas sensors. *Sens. Actuators B Chem.* **2012**, *175*, 163–172. [CrossRef]

32.   Suhak, Y.; Roshchupkin, D.; Redkin, B.; Kabir, A.; Jerliu, B.; Ganschow, S.; Fritze, H. Correlation of Electrical Properties and Acoustic Loss in Single Crystalline Lithium Niobate-Tantalate Solid Solutions at Elevated Temperatures. *Crystals* **2021**, *11*, 398. [CrossRef]

33.   Perini, N.; Prado, A.; Sad, C.; Castro, E.; Freitas, M. Electrochemical impedance spectroscopy for in situ petroleum analysis and water-in-oil emulsion characterization. *Fuel* **2012**, *91*, 224–228. [CrossRef]

34.   Dobromir, M.; Konrad-Soare, C.T.; Stoian, G.; Semchenko, A.; Kovalenko, D.; Luca, D. Surface Wettability of ZnO-Loaded TiO_2 Nanotube Array Layers. *Nanomaterials* **2020**, *10*, 1901. [CrossRef] [PubMed]

35.   Smecca, E.; Sanzaro, S.; Galati, C.; Renna, L.; Gervasi, L.; Santangelo, A.; Condorelli, G.G.; Grosso, D.; Bottein, T.; Mannino, G. Porous Gig-Lox TiO_2 Doped with N_2 at Room Temperature for P-Type Response to Ethanol. *Chemosensors* **2019**, *7*, 12. [CrossRef]

36. Saruhan, B.; Haidry, A.A.; Yüce, A.; Ciftyürek, E.; Mondragón Rodríguez, G.C. A Double Layer Sensing Electrode "BaTi$_{(1-X)}$ Rh$_x$O$_3$/Al-Doped TiO$_2$" for NO$_2$ Detection above 600 °C. *Chemosensors* **2016**, *4*, 8. [CrossRef]

37. Ruiz, A.M.; Sakai, G.; Cornet, A.; Shimanoe, K.; Morante, J.R.; Yamazoe, N. Cr-doped TiO$_2$ gas sensor for exhaust NO$_2$ monitoring. *Sens. Actuators B Chem.* **2003**, *93*, 509–518. [CrossRef]

38. Sivachandiran, L.; Thévenet, F.; Gravejat, P.; Rousseau, A. Investigation of NO and NO$_2$ adsorption mechanisms on TiO$_2$ at room temperature. *Appl. Catal. B Environ.* **2013**, *142*, 196–204. [CrossRef]

39. Hope, G.A.; Bard, A.J. Platinum/titanium dioxide (rutile) interface. Formation of ohmic and rectifying junctions. *J. Phys. Chem.* **1983**, *87*, 1979–1984. [CrossRef]

40. Zhu, Z.; Lin, S.-J.; Wu, C.-H.; Wu, R.-J.J.S.; Physical, A.A. Synthesis of TiO$_2$ nanowires for rapid NO$_2$ detection. *Sens. Actuators A Phys.* **2018**, *272*, 288–294. [CrossRef]

41. Mokrushin, A.S.; Simonenko, E.P.; Simonenko, N.P.; Bukunov, K.A.; Gorobtsov, P.Y.; Sevastyanov, V.G.; Kuznetsov, N.T. Gas-sensing properties of nanostructured TiO$_2$–xZrO$_2$ thin films obtained by the sol–gel method. *J. Sol-Gel Sci. Technol.* **2019**, *92*, 415–426. [CrossRef]